THE JOURNAL OF PHYSICAL CHEMISTRY Letters

Letter

pubs.acs.org/JPCL

Spontaneous Defect Annihilation in $CH_3NH_3PbI_3$ Thin Films at Room Temperature Revealed by Time-Resolved Photoluminescence Spectroscopy

Yasuhiro Yamada, Masaru Endo, Atsushi Wakamiya, and Yoshihiko Kanemitsu*

Institute for Chemical Research, Kyoto University, Uji, Kyoto 611-0011, Japan

ABSTRACT: We utilized time-resolved photoluminescence (PL) spectroscopy to investigate the photocarrier recombination dynamics in $CH_3NH_3PbI_3$ thin films as a function of the time elapsed from the film's fabrication. We found that the PL lifetime gradually increased and began to level out once the age of the film reached ~30 h. Even under weak excitation, the PL dynamics depended on the excitation intensity in the fresh sample, while the mature sample displayed no excitation-intensity dependence associated with the PL dynamics. We submit that this can be explained by the fact that a significant number of defects are initially formed in $CH_3NH_3PbI_3$ thin films fabricated by the sequential method and are spontaneously reduced by room-temperature annealing. Our results provide important insights for reducing the nonradiative recombination centers, which improves the power conversion efficiency of perovskite solar cells.

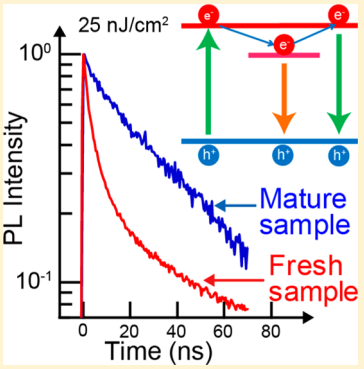

Lead halide perovskite semiconductors $CH_3NH_3PbX_3$ (X = Cl, Br, and I) recently demonstrated high power-conversion efficiency and ease of fabrication in photovoltaic applications, which together suggest significant potential as prospective solar-cell materials.[1−6] The conversion efficiency of perovskite-based solar cells is being improved at an unprecedentedly rapid pace (currently as high as 20.1%)[7] and is at par with that of other polycrystalline thin-film solar cells based on CdTe and copper indium gallium selenide (CIGS). Different types of perovskite solar cells have been reported so far,[1−4,8−10] the most-common structure being conformed to that of sensitized solar cells, in which a $CH_3NH_3PbI_3$ layer is deposited on a mesoporous film of TiO_2 through a sequential deposition method using solid hole-transporting materials.[5] Perovskite solar cells of this type display the highest reported conversion efficiency among perovskite solar cells. Planar heterojunction-type solar cells have also been fabricated by chemical vapor deposition and solution processes.[8−10] In these types of perovskite solar cells, the power conversion efficiency of cells ranges widely, even when fabricated by the same procedures.[11−14] Moreover, unusual and large current−voltage hysteresis of the perovskite solar cells has been observed, and its origins are still under discussion.[15−18] These factors suggest that small differences in the crystallinity of perovskite semiconductors, in addition to the interface conditions, might critically impact the photoconversion processes. However, our overall understanding of the factors that determine efficiency in perovskite solar cells still remains in a preliminary stage. Therefore, for further development of perovskite solar cells, it is requisite to gain a thorough understanding of the photo-conversion processes, along with their relationship to the fabrication processes.

Time-resolved optical spectroscopy is one of the most versatile techniques for evaluating the fundamental optical properties of this new class of solar-cell materials. The carrier-transport and carrier-recombination processes in $CH_3NH_3PbX_3$ have been extensively studied by means of time-resolved photoluminescence (PL) and transient absorption (TA) studies.[19−24] In a previous study, we revealed that the optical responses of $CH_3NH_3PbI_3$ films are determined by free photocarriers rather than excitons.[23] The carrier recombination process is dominated by the electron−hole radiative recombination under high-density excitation, while nonradiative recombination due to defects and impurities plays a dominant role under weak excitation.[21,23] In particular, nonradiative recombination gives rise to the loss of power conversion efficiency in solar cells.[25,26] $CH_3NH_3PbX_3$ semiconductors used in high-efficiency perovskite solar cells tend to display long PL lifetimes and high quantum yields because of small nonradiative recombination rates.[6]

We report on the gradual increase in carrier lifetime as a function of the time elapsed since $CH_3NH_3PbI_3$ thin-film fabrication (and under weak excitation conditions). This PL lifetime is shown to level out for samples measured ~30 h after fabrication and with a fixed excitation intensity. Moreover, we show that the PL lifetime of the fresh samples (i.e., <2 h old) is reduced with a decrease in excitation-intensity, whereas the PL lifetime of mature samples (i.e., more than 48 h old) shows no significant excitation-intensity dependence. In response to these results, we discuss the carrier recombination processes in fresh $CH_3NH_3PbI_3$ thin films in conjunction with the shallow defect

Received: December 17, 2014
Accepted: January 19, 2015
Published: January 19, 2015

DOI: 10.1021/jz5026596
J. Phys. Chem. Lett. 2015, 6, 482−486

states that are spontaneously annihilated, even at room temperature. We consider this defect-annihilation process to be the key factor that explains the superior performance of perovskite solar cells.

An efficient PL band is observed at ~1.60 eV in $CH_3NH_3PbI_3$ thin films at room temperature from an above-bandgap photoexcitation (E_g = 1.61 eV), as shown in the inset of Figure 1a. The PL spectrum shape is independent of

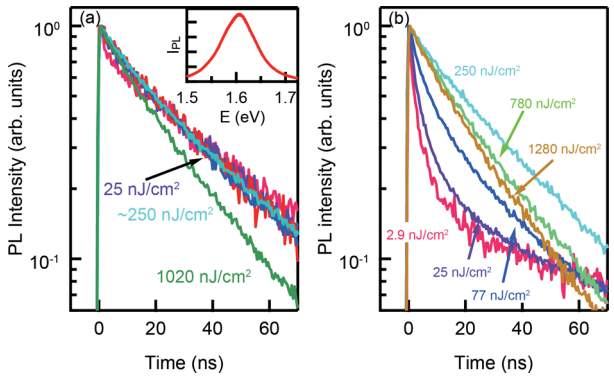

Figure 1. PL decay profiles at different excitation intensities in the $CH_3NH_3PbI_3$ thin film. (a) 48 h after fabrication (the mature sample) and (b) just after fabrication (the fresh sample). The inset shows the time-integrated PL spectrum of the $CH_3NH_3PbI_3$ thin film.

excitation intensity and photon energy. Figure 1a shows the PL decay profiles of $CH_3NH_3PbI_3$ thin films 48 h after fabrication and under different excitation intensities. The PL signal was monitored at ~1.60 eV. The PL dynamics show nearly monoexponential profiles and are almost independent of excitation intensity under weak excitation. (See Figure 2.) The PL decay becomes faster under strong excitation above 500 nJ/cm^2.

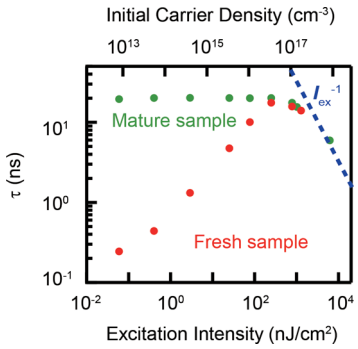

Figure 2. PL lifetime as a function of excitation intensity in the fresh sample and the mature sample. The blue dotted line shows an inverse linear relationship to excitation intensity. The initial photocarrier density is shown along the top axis.

Such excitation-intensity-dependent PL dynamics are consistent with our previous report.[23] More particularly, we have reported that the PL dynamics are well described by the following equations[23]

$$dn/dt = -An - Bn^2 \quad (1a)$$

$$I_{PL} \propto Bn^2 + BNn \quad (1b)$$

Here n is the photocarrier density. A and B represent the (Shockley–Read–Hall) carrier-trapping coefficient and the electron–hole radiative recombination coefficient, respectively. N is the carrier density caused by unintentional doping in the sample. According to these equations, the PL dynamics are determined by the electron–hole radiative recombination (Bn^2) under strong excitation, while the PL lifetime under weak excitation is $1/(2A)$,[27,28] independent of excitation intensity. It should be noted that A, which corresponds to the PL decay rate under weak excitation, differs from one sample to another because it is determined by the density of defects and impurities. We observed no significant sample dependence of B, which has been previously determined to be 1.7×10^{-10} s^{-1} cm^3.[23] We can estimate the PL quantum efficiency under weak excitation ($n \ll N$) as ~1% based on eqs 1a and 1b and previously reported values of A, B, and N.[23] We confirmed that the PL dynamics, monitored on the same excitation spot, remain unchanged for samples that are aged beyond 48 h.

Contrary to the case of the mature samples, the PL lifetimes of the fresh samples exhibit strong dependence on the excitation intensity even under weak excitation conditions, where electron–hole radiative recombination is negligible, as shown in Figure 1b. Under very weak excitation (e.g., 2.9 nJ/cm^2), the PL decay profile shows fast and slow components. With an increase in excitation intensity, the lifetime of fast PL component becomes longer and the slow component is reduced. Under an excitation intensity of 250 nJ/cm^2, the PL dynamics display nearly monoexponential behavior and agree well with those of the mature sample. However, when the excitation intensity exceeds 500 nJ/cm^2, the PL lifetime begins to be reduced as excitation intensity increases, showing no difference in PL decay curves between the fresh and the mature samples. It is worth mentioning that 500 nJ/cm^2 corresponds to the time-averaged power density of 100 mW/cm^2, which is almost the same as solar radiation power density (AM 1.5). Because the photogenerated carrier density just after the pulse excitation is much higher than that under continuous-wave excitation with the same average power density, we consider that the excitation level (0.1 nJ/cm^2 to 1 μJ/cm^2) is relevant to the actual device operation.

The PL lifetime as a function of excitation intensity is summarized in Figure 2. Here we define the PL lifetime, τ, such that $I_{PL}(\tau) = I_{PL}(0)/e$, where $I_{PL}(t)$ is the PL intensity at time t after photoexcitation. The initial photocarrier density calculated using the optical absorption coefficient at 1.8 eV is also shown on the top axis of this Figure. The PL lifetime of the mature sample shows a constant value under weak excitation (i.e., <500 nJ/cm^2). Under strong excitation, the PL lifetime becomes inversely proportional to the excitation intensity due to the electron–hole radiative recombination.

The PL lifetime of the fresh sample is much shorter than that of the mature sample, even under weak excitation. With an increase in excitation intensity below 500 nJ/cm^2, the PL lifetime monotonically increases and approaches the PL lifetime of the mature sample. These observations suggest that an additional relaxation channel of photocarriers exists in the fresh samples, that it saturates under high-intensity excitation, and that it comes to be attenuated with an increase in the time elapsed after thin-film fabrication.

To explain the mechanism of anomalous PL dynamics in the fresh films, we must consider the finite number of shallow trapping centers. Under weak excitation, the photoexcited carriers are rapidly trapped into shallow states, which results in the rapid PL decay. A fraction of trapped carriers is thermally upconverted to the band-edge state, and the others recombine

DOI: 10.1021/jz5026596
J. Phys. Chem. Lett. 2015, 6, 482–486

nonradiatively. The thermal excitation from shallow states to band-edge states causes a slow PL decay component. With an increase in the population of photocarriers, the shallow states are more fully occupied, thereby reducing the trapping rate of the carriers.

It is reasonable to assume that defects formed in $CH_3NH_3PbI_3$ thin films give rise to the shallow states because $CH_3NH_3PbI_3$ thin-film samples fabricated by the sequential method might contain a large number of defects. In this fabrication method, unreacted CH_3NH_3I and PbI_2 are mixed in the sample because the thermodynamically stable range for equilibrium growth of $CH_3NH_3PbI_3$ is quite narrow according to theoretical studies.[29] Therefore, nonstoichiometric (or defect-rich) $CH_3NH_3PbI_3$ thin films might be formed just after fabrication. Because the excitation-intensity dependence disappears in the mature sample, the room-temperature annealing process might reduce the trapping rate of photocarriers to defects. In other words, the defect states are spontaneously annihilated even at room temperature. It is our view that the chemical reaction of unreacted compounds gradually makes progress in the defect-rich $CH_3NH_3PbI_3$ thin films. It is worth mentioning that we annealed the sample after sequential deposition of $CH_3NH_3PbI_3$ perovskite layer at 70 °C for 1 h. (See the Experimental Methods.)

To better understand the dynamical behaviors of the fresh sample, we studied the temporal variation of PL dynamics under a fixed excitation intensity of 40 nJ/cm^2, where the PL lifetime is determined by the carrier trapping process previously mentioned. Typical data are shown in Figure 3a. As shown in

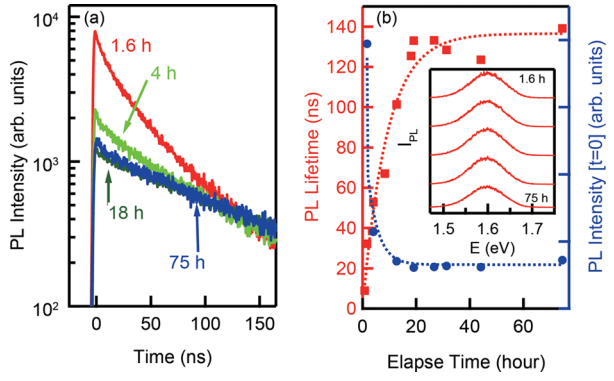

Figure 3. (a) Temporal variation of PL dynamics under an excitation intensity of 40 nJ/cm^2. (b) PL lifetime and initial PL intensity as a function of elapsed time after fabrication. The dotted curves are fitting results by a double-exponential function. The inset shows the PL spectra at different elapsed times (1.6 to 75 h) after fabrication.

Figure 3b, the PL lifetime lengthens as time elapses and reaches a constant value typically after ~30 h. The PL intensity at zero delay time (initial PL intensity) decreases more rapidly compared with PL lifetime. It should be noted that the relaxation times of PL lifetime and intensity also vary from sample to sample.

The inset of Figure 3b illustrates that the PL spectrum shape is independent of elapsed time, whereas the PL dynamics and intensity change with time. This result indicates that the PL mechanism remains unchanged with elapsed time after fabrication. According to eq 1b, the initial PL intensity is determined by BN under weak excitation. It has been reported that the B coefficient and PL spectrum shape simultaneously change through crystal morphology.[30] Because no time variation of PL spectrum is observed, it is considered that B coefficient is also unchanged. Alternatively, we consider that N is rapidly reduced within a few hours after fabrication because unintentionally doped carriers are supplied by vacancies and impurities in the sample.[27,28,31] On the basis of these results, we can isolate two origins of temporal variation of PL properties: the defect annihilation and the reduction of unintentionally doped carrier density. Furthermore, we believe that these two mechanisms are closely linked to each other.

To confirm the slowly developing chemical reaction of unreacted compounds in the thin film samples, it is significant to measure the time-variation of optical absorption spectra. The inset of Figure 4a shows the optical density spectra in the range

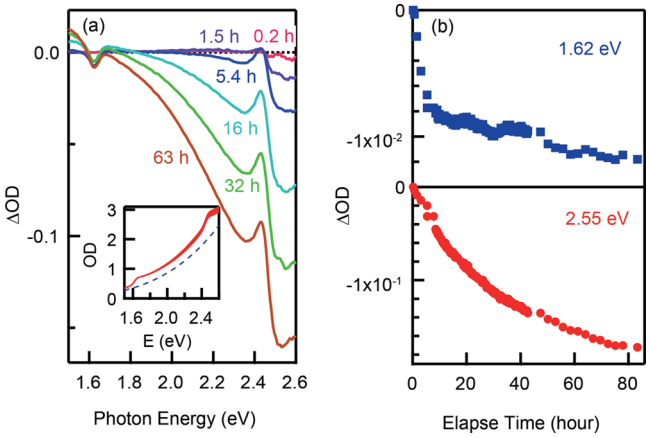

Figure 4. (a) Difference spectra of optical density at different elapse times. The inset shows the optical density spectra. The eye-guide (dotted curve) shows the background component due to light scattering. (b) Temporal changes of optical density at 1.62 and 2.55 eV.

between 1.5 and 2.6 eV. The background component increasing toward high energy side, indicated by the dotted curve, is caused by light scattering from the sample. The absorption onsets at 1.6 and 2.4 eV correspond to band edge of $CH_3NH_3PbI_3$ and PbI_2, respectively.[22,32] Figure 4a shows the changes of optical density after sample fabrication, $\Delta OD(t) = OD(t) - OD(0)$, where $OD(t)$ is the optical density spectrum at elapse time t. The optical absorption of PbI_2 clearly decreases with the elapsed time, indicating that chemical reaction of unreacted PbI_2 occurs. The difference spectrum shows a peak at 1.62 eV, the band edge of $CH_3NH_3PbI_3$. This means that the optical absorption edge becomes steeper and the Urbach tail is reduced, suggesting that the crystal quality is improved with elapse time. Figure 4b shows the time variation of optical density at 1.62 eV ($CH_3NH_3PbI_3$) and 2.55 eV (PbI_2). While optical density at 1.62 eV rapidly decreases, relatively slow temporal change is observed at 2.55 eV. These behaviors are consistent with the two decay components in PL properties, as shown in Figure 3b.

The defect-annihilation effect via room-temperature annealing should be related to microcrystalline grains of $CH_3NH_3PbI_3$ thin films fabricated by the sequential method.[5] The crystal and surface morphology of the $CH_3NH_3PbI_3$ thin-film layer have recently been discussed as critical issues of perovskite solar cells.[10,16] This situation is similar to that observed in other thin-film solar cell materials, such as CIGS, copper zinc tin sulfide (CZTS), and CdTe.[33−37] For these materials, the physical mechanisms that suppress the nonradiative recombination of

DOI: 10.1021/jz5026596
J. Phys. Chem. Lett. 2015, 6, 482−486

photocarriers at the grain surfaces have been discussed.[33−37] We submit that the spontaneous defect annihilation is essential for the high photoconversion efficiency of $CH_3NH_3PbI_3$-based perovskite solar cells, despite their microcrystalline grain structures. Our findings provide important insights relevant to improving the efficiency of perovskite solar cells. By utilizing the gradual change of the properties in $CH_3NH_3PbI_3$, it is expected that a new fabrication method to obtain high-quality perovskite layers can be developed.

Finally, the spontaneous defect annihilation seems to be intimately connected to solar cell efficiency. To examine this connection, we fabricated $CH_3NH_3PbI_3$-based solar cells by a standard sequential method (see ref 11 for details): The perovskite layer is formed by dipping the PbI_2 layer on mesoporous TiO_2 into a CH_3NH_3I solution, and hole-transporting material (spiro-OMeTAD) is deposited onto it. We prepared different samples by changing the elapsed time from the perovskite-layer deposition to the hole-transporting material deposition. In some cases, the power conversion increased with the time elapsed between these two steps. In particular, this effect seems to be pronounced when the initial power conversion efficiency is low ($\eta \approx 8\%$). Figure 5 shows typical histograms of open-circuit voltage (V_{OC}), short-circuit current (J_{SC}), and power conversion efficiency under AM1.5 excitation for low-efficiency cells.

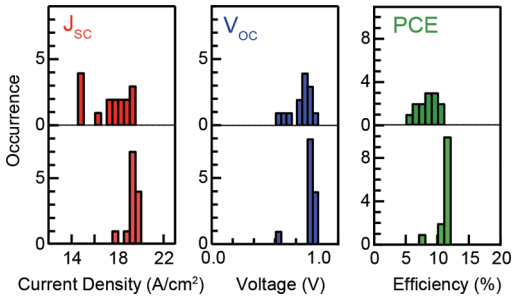

Figure 5. Typical histogram of open-circuit voltage (V_{OC}), short-circuit current (J_{SC}), and power conversion efficiency (PCE) of $CH_3NH_3PbI_3$-based solar cells under AM1.5 excitation for low-efficiency cells. Two groups of solar cells were compared: one was fabricated by a standard sequential method (top pane in each histogram). In the fabrication of the other group (bottom pane in each histogram), we waited until 12 h after the formation of the $CH_3NH_3PbI_3$ layer to deposit the hole-transporting spiro-OMeTAD.

The power conversion increased by waiting to deposit the hole-transporting materials until 12 h after fabricating the perovskite layer. We argue that defect density in the perovskite layer comes to be reduced as time elapses, resulting in the reduction of nonradiative photocarrier recombination and efficiency improvement. However, high-efficiency cells ($\eta \approx$ >12%) do not display time-dependent efficiency. Accordingly, the conversion efficiency in such high-efficiency cells should be primarily determined by the other factors, such as defect density, flatness at the interface of perovskite and hole-transporting materials, and the quality of the perovskite layer.

In conclusion, we investigated the PL dynamics of $CH_3NH_3PbI_3$ thin films. We analyzed the time variation of the PL lifetime in conjunction with reducing the nonradiative recombination rate due to defects in the samples by room-temperature thermal annealing effects. The defect annihilation at room temperature seems to be related to the microcrystalline grain formation in $CH_3NH_3PbI_3$ thin films. By utilizing the defect annihilation effects in $CH_3NH_3PbI_3$, a better fabrication method to obtain high-quality perovskite layers can be developed. Our results therefore provide useful insights for improving the quality of perovskite semiconductors, which can lead to power conversion efficiency enhancement of perovskite solar cells.

EXPERIMENTAL METHODS

We fabricated $CH_3NH_3PbI_3$ films on SiO_2 glass substrates by a sequential deposition method[6] in an inert glovebox (Ar, H_2O, and O_2,< 0.1 ppm) using dehydrated (H_2O < 8 ppm) solvents and PbI_2 (H_2O < 100 ppm). Our use of dehydrated materials enabled the highly reproducible fabrication of solar cells.[38] PbI_2 thin films were deposited on the substrate by spin-coating. The samples were dipped into CH_3NH_3I solution and annealed at 70 °C for 1 h. (See ref 23 for further details.) Samples were kept in transparent acryl boxes filled with Ar gas before and during measurements to keep the samples from being exposed to air, thereby preventing the degradation caused by O_2 and humidity. Time-resolved PL measurements were conducted with a monochromator and a streak camera. The time resolution of the PL measurement was 50 ps. We used a picosecond-pulsed laser diode (repetition rate: 200 kHz, pulse width: 20 ps, photon energy: 1.80 eV) as an excitation light source. All experiments were conducted at room temperature.

AUTHOR INFORMATION

Corresponding Author

*E-mail: kanemitu@scl.kyoto-u.ac.jp.

Notes

The authors declare no competing financial interest.

ACKNOWLEDGMENTS

Part of this work was supported by the Sumitomo Electric Industries Group CSR Foundation (to Y.Y. and Y.K.), JST-PRESTO (to A.W.), and JST-CREST (to Y.K.).

REFERENCES

(1) Kojima, A.; Teshima, K.; Shirai, Y.; Miyasaka, T. Organometal Halide Perovskites as Visible-Light Sensitizers for Photovoltaic Cells. *J. Am. Chem. Soc.* **2009**, *131*, 6050−6051.

(2) Im, J. H.; Lee, C. R.; Lee, J. W.; Park, S. W.; Park, N. G. 6.5% Efficient Perovskite Quantum-Dot-Sensitized Solar Cell. *Nanoscale* **2011**, *3*, 4088−4093.

(3) Kim, H. S.; Lee, C. R.; Im, J. H.; Lee, K. B.; Moehl, T.; Marchioro, A.; Moon, S. J.; Humphry-Baker, R.; Yum, J. H.; Moser, J. E.; Grätzel, M.; Park, N. G. Lead Iodide Perovskite Sensitized All-Solid-State Submicron Thin Film Mesoscopic Solar Cell with Efficiency Exceeding 9%. *Sci. Rep.* **2012**, *2*, 591.

(4) Lee, M. M.; Teuscher, J.; Miyasaka, T.; Murakami, T. N.; Snaith, H. J. Efficient Hybrid Solar Cells Based on Meso-Superstructured Organometal Halide Perovskites. *Science* **2012**, *338*, 643−647.

(5) Burschka, J.; Pellet, N.; Moon, S.-J.; Humphry-Baker, R.; Gao, P.; Nazeeruddin, M. K.; Gratzel, M. Sequential Deposition As a Route to High-Performance Perovskite-Sensitized Solar Cells. *Nature* **2013**, *499*, 316−319.

(6) Zhou, H.; Chen, Q.; Li, G.; Luo, S.; Song, T.; Duan, H.; Hong, Z.; You, J.; Liu, Y.; Yang, Y. Interface Engineering of Highly Efficient Perovskite Solar Cells. *Science* **2014**, *345*, 542−546.

(7) Best Research Cell Efficiency Chart. http://www.nrel.gov/ncpv/images/efficiency_chart.jpg.

(8) Docampo, P.; Ball, J. M.; Darwich, M.; Eperon, G. E.; Snaith, H. J. Efficient Organometal Trihalide Perovskite Planar-heterojunction Solar Cells on Flexible Polymer Substrates. *Nat. Commun.* **2013**, *4*, 2761.

DOI: 10.1021/jz5026596
J. Phys. Chem. Lett. 2015, 6, 482−486

(9) Liu, M.; Johnston, M. B.; Snaith, H. J. Efficient Planar Heterojunction Perovskite Solar Cells by Vapour Deposition. *Nature* **2013**, *501*, 395−398.
(10) Eperon, G. E.; Burlakov, V. M.; Docampo, P.; Goriely, A.; Snaith, H. J. Morphological Control for High Performance, Solution-Processed Planar Heterojunction Perovskite Solar Cells. *Adv. Funct. Mater.* **2014**, *24*, 151−157.
(11) Heo, J. H.; Im, S. H.; Noh, J. H.; Mandal, T. N.; Lim, C.-S.; Chang, J. A.; Lee, Y. H.; Kim, H.; Sarkar, A.; Nazeeruddin, Md. K.; et al. Efficient Inorganic−organic Hybrid Heterojunction Solar Cells Containing Perovskite Compound and Polymeric Hole Conductors. *Nat. Photonics* **2013**, *7*, 486−491.
(12) Lee, J.-W.; Lee, T.-Y.; Yoo, P. J.; Grätzel, M.; Mhaisalkard, S.; Park, N.-G. Rutile TiO_2-based Perovskite Solar Cells. *J. Mater. Chem. A* **2014**, *2*, 9251−9259.
(13) Liu, D.; Kelly, T. L. Perovskite Solar Cells With a Planar Heterojunction Structure Prepared Using Room-temperature Solution Processing Techniques. *Nat. Photonics* **2014**, *8*, 133−138.
(14) Hao, F.; Stoumpos, C. C.; Liu, Z.; Chang, R. P. H.; Kanatzidis, M. G. Controllable Perovskite Crystallization at a Gas−Solid Interface for Hole Conductor-Free Solar Cells with Steady Power Conversion Efficiency over 10%. *J. Am. Chem. Soc.* **2014**, *136*, 16411−16419.
(15) Snaith, H. J.; Abate, A.; Ball, J. M.; Eperon, G. E.; Leijtens, T.; Noel, N. K.; Stranks, S. D.; Wang, J. T.; Wojciechowski, K.; Zhang, W. Anomalous Hysteresis in Perovskite Solar Cells. *J. Phys. Chem. Lett.* **2014**, *5*, 1511−1515.
(16) Kim, H.-S.; Park, N.-G. Parameters Affecting I−V Hysteresis of $CH_3NH_3PbI_3$ Perovskite Solar Cells: Effects of Perovskite Crystal Size and Mesoporous TiO_2 Layer. *J. Phys. Chem. Lett.* **2014**, *5*, 2927−2934.
(17) Jeon, N. J.; Noh, J. H.; Kim, Y. C.; Yang, W. S.; Ryu, S.; Seok, S. I. Solvent Engineering for High-performance Inorganic−organic Hybrid Perovskite Solar Cells. *Nat. Mater.* **2014**, *13*, 897−903.
(18) Wei, J.; Zhao, Y.; Li, H.; Li, G.; Pan, J.; Xu, D.; Zhao, Q.; Yu, D. Hysteresis Analysis Based on the Ferroelectric Effect in Hybrid Perovskite Solar Cells. *J. Phys. Chem. Lett.* **2014**, *5*, 3937−3945.
(19) Stranks, S. D.; Eperon, G. E.; Grancini, G.; Menelaou, C.; Alcocer, M. J. P.; Leijtens, T.; Herz, L. M.; Petrozza, A.; Snaith, H. J. Electron-Hole Diffusion Lengths Exceeding 1 Micrometer in an Organometal Trihalide Perovskite Absorber. *Science* **2013**, *342*, 341−344.
(20) Xing, G.; Mathews, N.; Sun, S.; Lim, S. S.; Lam, Y. M.; Grätzel, M.; Mhaisalkar, S.; Sum, T. C. Long-Range Balanced Electron- and Hole-Transport Lengths in Organic-Inorganic $CH_3NH_3PbI_3$. *Science* **2013**, *342*, 344−347.
(21) Deschler, F.; Price, M.; Pathak, S.; Klintberg, L. E.; Jarausch, D.-D.; Higler, R.; Hüttner, S.; Leijtens, T.; Stranks, S. D.; Snaith, H. J.; et al. High Photoluminescence Efficiency and Optically Pumped Lasing in Solution-Processed Mixed Halide Perovskite Semiconductors. *J. Phys. Chem. Lett.* **2014**, *5*, 1421−1426.
(22) Yamada, Y.; Nakamura, T.; Endo, M.; Wakamiya, A.; Kanemitsu, Y. Near-Band-Edge Optical Responses of Solution-Processed Organic−Inorganic Hybrid Perovskite $CH_3NH_3PbI_3$ on Mesoporous TiO_2 Electrodes. *Appl. Phys. Express* **2014**, *7*, 032302.
(23) Yamada, Y.; Nakamura, T.; Endo, M.; Wakamiya, A.; Kanemitsu, Y. Photocarrier Recombination Dynamics in Perovskite $CH_3NH_3PbI_3$ for Solar Cell Applications. *J. Am. Chem. Soc.* **2014**, *136*, 11610−11613.
(24) Yamada, Y.; Nakamura, T.; Endo, M.; Wakamiya, A.; Kanemitsu, Y. Photoelectronic Responses in Solution-Processed Perovskite $CH_3NH_3PbI_3$ Solar Cells Studied by Photoluminescence and Photoabsorption Spectroscopy. *IEEE J. Photovoltaics* **2015**, *5*, 401−405.
(25) Miller, O. D.; Yablonovitch, E.; Kurtz, S. R. Strong Internal and External Luminescence as Solar Cells Approach the Shockley−Queisser Limit. *IEEE J. Photovoltaics* **2012**, *2*, 303−311.
(26) Zhu, L.; Kim, C.; Yoshita, M.; Chen, S.; Sato, S.; Mochizuki, T.; Akiyama, H.; Kanemitsu, Y. Impact of Sub-cell Internal Luminescence Yields on Energy Conversion Efficiencies of Tandem Solar Cells: A Design Principle. *Appl. Phys. Lett.* **2014**, *104*, 031118.
(27) Yasuda, H.; Kanemitsu, Y. Dynamics of Nonlinear Blue Photoluminescence and Auger Recombination in $SrTiO_3$. *Phys. Rev. B* **2008**, *77*, 193202.
(28) Yamada, Y.; Yasuda, H.; Tayagaki, T.; Kanemitsu, Y. Temperature Dependence of Photoluminescence Spectra of Undoped and Electron-Doped $SrTiO_3$: Crossover from Auger Recombination to Single-Carrier Trapping. *Phys. Rev. Lett.* **2009**, *102*, 247401.
(29) Yin, W.-J.; Shi, T.; Yan, Y. Unusual Defect Physics in $CH_3NH_3PbI_3$ Perovskite Solar Cell Absorber. *Appl. Phys. Lett.* **2014**, *104*, 063903.
(30) D'Innocenzo, V.; Kandada, A. R. S.; De Bastiani, M.; Gandini, M.; Petrozza, A. Tuning the Light Emission Properties by Band Gap Engineering in Hybrid Lead Halide Perovskite. *J. Am. Chem. Soc.* **2014**, *136*, 17730−17733.
(31) Yasuda, H.; Yamada, Y.; Tayagaki, T.; Kanemitsu, Y. Spatial Distribution of Carriers in $SrTiO_3$ Revealed by Photoluminescence Dynamics Measurements. *Phys. Rev. B* **2008**, *78*, 33202.
(32) Sandroff, C. J.; Hwang, D. M.; Chung, W. M. Carrier Confinement and Special Crystallite Dimensions in Layered Semiconductor Colloids. *Phys. Rev. B* **1986**, *33*, 5953(R).
(33) Persson, C.; Zunger, A. Anomalous Grain Boundary Physics in Polycrystalline $CuInSe_2$: The Existence of a Hole Barrier. *Phys. Rev. Lett.* **2003**, *91*, 266401.
(34) Visoly-Fisher, I.; Cohen, S. R.; Ruzin, A.; Cahen, D. How Polycrystalline Devices Can Outperform Single-Crystal Ones: Thin Film CdTe/CdS Solar Cells. *Adv. Mater.* **2004**, *16*, 879.
(35) Persson, C.; Zunger, A. Compositionally Induced Valence-Band Offset at the Grain Boundary of Polycrystalline Chalcopyrites Creates a Hole Barrier. *Appl. Phys. Lett.* **2005**, *87*, 211904.
(36) Yan, Y.; Noufi, R.; Al-Jassim, M. M. Grain-Boundary Physics in Polycrystalline $CuInSe_2$ Revisited: Experiment and Theory. *Phys. Rev. Lett.* **2006**, *96*, 205501.
(37) Yin, W.-J.; Wu, Y.; Wei, S.-H.; Noufi, R.; Al-Jassim, M. M.; Yan, Y. Engineering Grain Boundaries in $Cu_2ZnSnSe_4$ for Better Cell Performance: A First-Principle Study. *Adv. Energy Mater.* **2014**, *4*, 1300712.
(38) Wakamiya, A.; Endo, M.; Sasamori, T.; Tokitoh, N.; Ogomi, Y.; Hayase, S.; Murata, Y. Reproducible Fabrication of Efficient Perovskite-Based Solar Cells: X-ray Crystallographic Studies on the Formation of $CH_3NH_3PbI_3$ Layers. *Chem. Lett.* **2014**, *43*, 711−713.

DOI: 10.1021/jz5026596
J. Phys. Chem. Lett. 2015, 6, 482−486